Letter

Damped Dirac magnon in the metallic kagome antiferromagnet FeSn

Seung-Hwan Do,[1] Koji Kaneko,[2,3] Ryoichi Kajimoto,[2] Kazuya Kamazawa,[4] Matthew B. Stone,[5] Jiao Y. Y. Lin,[6] Shinichi Itoh,[2,7] Takatsugu Masuda,[8,7] German D. Samolyuk,[1] Elbio Dagotto,[1,9] William R. Meier,[1] Brian C. Sales,[1] Hu Miao,[1] and Andrew D. Christianson[1]

[1]*Materials Science and Technology Division, Oak Ridge National Laboratory, Oak Ridge, Tennessee 37831, USA*
[2]*Materials and Life Science Division, J-PARC Center, Tokai, Ibaraki 319-1195, Japan*
[3]*Materials Sciences Research Center, Japan Atomic Energy Agency, Tokai, Ibaraki 319-1195, Japan*
[4]*Neutron Science and Technology Center, Comprehensive Research Organization for Science and Society, Tokai, Ibaraki 319-1106, Japan*
[5]*Neutron Scattering Division, Oak Ridge National Laboratory, Oak Ridge, Tennessee 37831, USA*
[6]*Second Target Station, Oak Ridge National Laboratory, Oak Ridge, Tennessee 37831, USA*
[7]*Institute of Materials Structure Science, High Energy Accelerator Research Organization, Tsukuba, Ibaraki 305-0081, Japan*
[8]*Institute for Solid State Physics, The University of Tokyo, Chiba 277-8581, Japan*
[9]*Department of Physics and Astronomy, University of Tennessee, Knoxville, Tennessee 37996, USA*

(Received 18 July 2021; revised 18 January 2022; accepted 6 April 2022; published 6 May 2022; corrected 1 August 2022)

The kagome lattice is a fertile platform to explore topological excitations with both Fermi-Dirac and Bose-Einstein statistics. While relativistic Dirac fermions and flat bands have been discovered in the electronic structure of kagome metals, the spin excitations have received less attention. Here, we report inelastic neutron scattering studies of the prototypical kagome magnetic metal FeSn. The spectra display well-defined spin waves extending to 120 meV. Above this energy, the spin waves become progressively broadened, reflecting interactions with the Stoner continuum. Using linear spin-wave theory, we determine an effective spin Hamiltonian that reproduces the measured dispersion. This analysis indicates that the Dirac magnon at the K point remarkably occurs on the brink of a region where well-defined spin waves become unobservable. Our results emphasize the influential role of itinerant carriers on the topological spin excitations of metallic kagome magnets.

DOI: 10.1103/PhysRevB.105.L180403

The interplay between charge, spin, and geometric frustration is an important underlying theme to problems at the forefront of condensed matter physics [1–9]. Kagome magnets, consisting of a corner-shared triangular network [Fig. 1(a)], are an ideal platform to explore correlated topological states, including the fractional quantum Hall effect [1–4], the intrinsic Chern state [9–12], and magnetic Weyl semimetals [13]. While the charge excitations of kagome magnets have been extensively investigated [5,5,6,8,9,13–16], their magnetic counterparts and the intertwined correlations between charge and spin degrees of freedom have not yet been investigated in detail.

In analogy to the electronic band structure for the single-orbital tight-binding model of a kagome lattice, linear spin-wave theory for the nearest-neighbor Heisenberg exchange (J_1) model for a kagome ferromagnetic spin lattice yields a Dirac magnon at the K point and a flat magnon band [Fig. 1(c)] [17–20]. Time-reversal symmetry-breaking interactions, such as the Dzyaloshinskii-Moriya interaction in magnetic insulators, introduce a gap at the Dirac point and can induce a topological thermal Hall effect [18–22]. In addition, magnon-magnon interactions may modify the dispersion to realize interaction-stabilized topological magnons [23,24]. This simplified picture is, however, challenged in a metallic kagome magnet, where the presence of itinerant electrons will introduce long-range magnetic interactions through, e.g., Ruderman-Kittel-Kasuya-Yosida (RKKY) interactions, that dramatically change the magnon dispersion as shown in Fig. 1(d). Moreover, the high-energy spin-wave excitations will interact with the particle-hole continuum of the Stoner excitation [Fig. 1(e)], resulting in mode decay.

To explore the effects of itinerant carriers on the magnons in the ferromagnetic kagome spin lattice, we study the spin excitation spectra of the metallic kagome magnet FeSn using inelastic neutron scattering (INS). The measured spectra show relatively sharp spin waves of the ferromagnetic kagome spin lattice below 120 meV. At higher energies, the spin waves exhibit decay due to interactions with the Stoner continua. Interestingly, we find that while the Dirac magnon remains, the upper branch of the Dirac band is heavily damped, uncovering a nontrivial interplay between the magnon and continuum.

FeSn crystallizes in a hexagonal structure ($P6/mmm$) with the Fe atoms forming a kagome spin lattice [Fig. 1(b)]. Below $T_N = 365$ K, the Fe spins form ferromagnetic kagome layers which are stacked antiferromagnetically along the c axis with an ordering wave vector of $\mathbf{Q}_m = (0, 0, 1/2)$. As we show in this Letter, the dominant in-plane ferromagnetic interactions allow the behavior of the quasi-two-dimensional ferromagnetic kagome spin lattice to be probed. For the INS measurements, 4.43 g of FeSn single crystals were coaligned on aluminum plates with a $[H, 0, L]$ horizontal scattering plane. The INS data were obtained at $T = 100$ K using the

 ©2022 American Physical Society

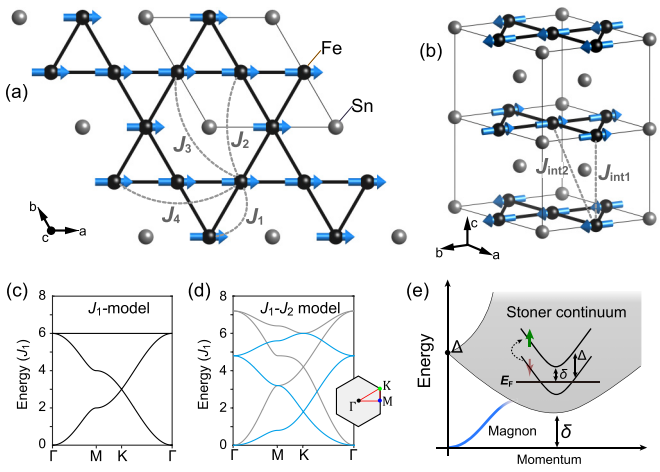

FIG. 1. (a), (b) Crystal and magnetic structure of FeSn. The exchange paths between Fe spins are indicated. (c), (d) The spin-wave dispersions of a ferromagnetic kagome lattice with $J_1 = -1$ meV and (c) $J_2 = 0$ and (d) $J_2 = 0.2J_1$ ($J_2 = -0.2J_1$), are displayed with black and gray (blue) curves, respectively. High-symmetry points are indicated in the inset to (d). (e) Schematic of a Stoner excitation spectra (continuum) and magnon (sharp dispersion) as a function of momentum (**Q**) and energy (E). The spin-wave mode decays into a particle-hole pair near the Fermi energy (E_F) when it enters the Stoner continuum. The continuum boundary shifts with gap Δ (δ), reflecting the direct (indirect) electronic transitions, as shown in the inset.

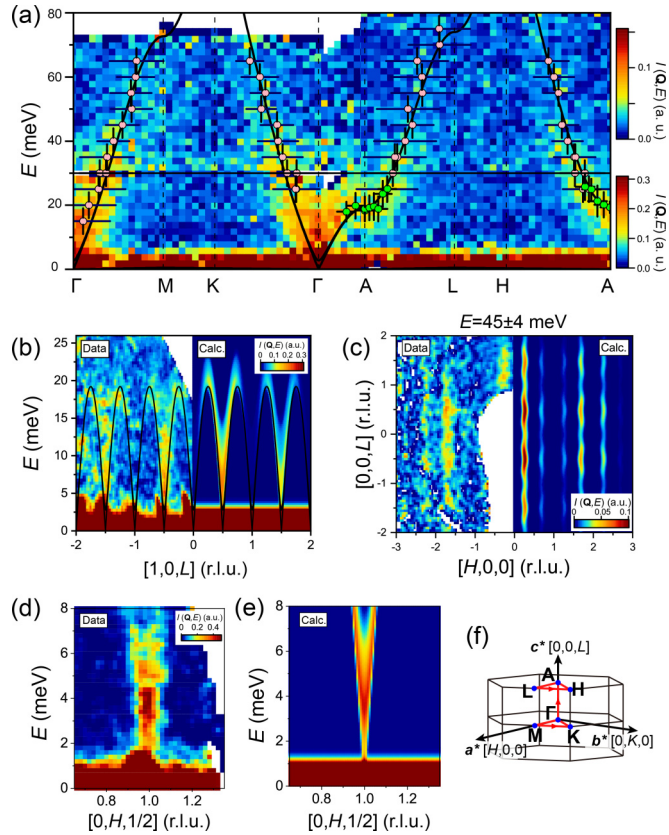

FIG. 2. (a) Contour map of the INS intensity along high-symmetry directions [given in (f)]. The data [(a), (c)] were measured using HRC with $E_i = 153$ meV. The spectrum above (below) the horizontal line at 30 meV was obtained from the BZ for Γ at $\mathbf{Q} = (0, 0, 1/2)$ [$(0, 0, 3/2)$], integrating over $Q = \pm 0.22$ Å^{-1} along the vertical direction. Horizontal (vertical) error bars of pink (green) circles indicate the fitted peaks full width at half maxima (FWHM), and vertical (horizontal) error bars indicate the range of energy (momentum) integration. (b) INS data (left) and spin-wave calculations (right) as described in the text along the out-of-plane direction through the Zone Center (ZC), measured using the 4SEASONS spectrometer with $E_i = 46$ meV. The solid line is the calculated magnon dispersion. (c) Constant energy slice of the magnon spectra in the $[H, 0, L]$ plane and the calculated spectra. (d) Low-energy spectrum of $I(\mathbf{Q}, E)$ near the ZC measured using $E_i = 27$ meV at 4SEASONS, and (e) the corresponding calculation including an easy-plane anisotropy of $SD_z = 0.1$ meV.

High Resolution Chopper (HRC) [25] (incident energies $E_i =$ 40 and 153 meV) and 4SEASONS [26] ($E_i = 27$, 46, 96, and 300 meV) spectrometers at the Japan Proton Accelerator Research Complex (J-PARC). Additional data [27] were collected with the SEQUOIA [28] spectrometer ($E_i = 500$ meV) at the Spallation Neutron Source (SNS) at Oak Ridge National Laboratory (see Supplemental Material [29] for additional details).

Figure 2 shows the spectra in the three-dimensional hexagonal Brillouin zone (BZ), measured by INS. The acoustic magnons emanate from $\mathbf{Q}_m = \Gamma(0, 0, 1/2)$, and disperse throughout the entire BZ. Strongly dispersive magnons in the HK plane extend well above 80 meV, whereas the magnon dispersion along the out-of-plane direction has a bandwidth of less than 20 meV, indicating the dominant spin-spin interactions are within the kagome-lattice planes. The nearly two-dimensional character of the spin excitation spectrum is further evidenced by the rodlike scattering shown in Fig. 2(c).

The high-energy spectra were measured using the SEQUOIA spectrometer with $E_i = 500$ meV. We integrate the INS data over $-4 \leqslant L \leqslant 4$ r.l.u. (reciprocal lattice units) to enhance statistics. Note that due to momentum and energy conservation, high-energy transfer data are obtained from a larger magnitude L region, which results in lower scattering intensity from the magnetic form factor contribution. As shown in Fig. 3, the excitations extend to at least 200 meV. Two individual magnon branches are observed corresponding to the lower- and mid-magnon bands in Fig. 1(c) of the ferromagnetic kagome spin lattices through the M and K points. The higher-energy spectral weight above ∼120 meV is diffuse, and becomes indiscernible from the background above ∼200 meV. Figure 3(c) shows momentum scans through Γ′-M-Γ-K-X for increasing energy transfer. Along both the Γ-M and Γ-K directions, the peak linewidths broaden as a function of **Q** near the zone boundary (ZB), and the peak positions are intact over a wide energy range $120 < E < 170$ meV ($80 < E < 120$ meV) near the K (M) point. The energy scans shown in Fig. 4(h) and Fig. S5 in the Supplemental Material [29] display linewidths considerably broader than the instrumental resolution. These peak broadenings in **Q** and E space indicate the decay of the magnons, resulting from quasiparticle scattering [30–32]. Considering the metallicity of FeSn along with the collinear spin configuration, FeSn

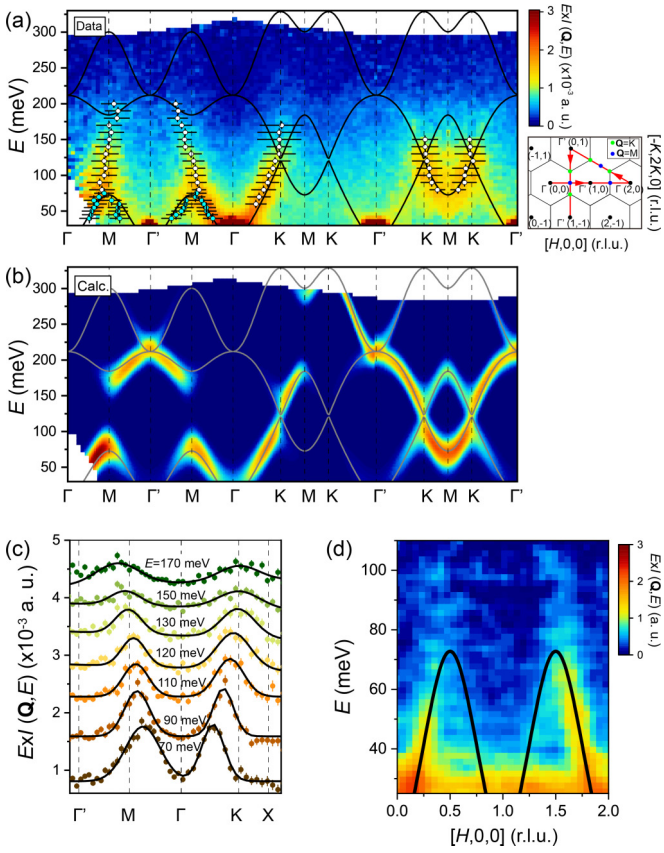

FIG. 3. (a) High-energy INS spectra [plotted as $E \times I(\mathbf{Q}, E)$] and (b) spin-wave calculations, along the high-symmetry directions as indicated in the right panel of the HK-reciprocal space map. Data were obtained by integrating over $Q = \pm 0.19$ Å^{-1} and $-4 \leqslant L \leqslant 4$. The calculation was performed for an identical $\mathbf{Q}$-integration range and convoluted with the instrumental resolution of SEQUOIA. The black solid lines display the magnon dispersion for $L = 0.5$. Horizontal (vertical) error bars of white solid circles indicate the fitted peaks FWHM (range of energy integration). (c) Constant energy cut along the high-symmetry directions, integrated over energy ± 5 meV. Solid lines are Gaussian fits described in the text with fitted values displayed in (a). (d) INS spectra obtained from HRC ($E_i = 153$ meV), integrated over $-3 \leqslant L \leqslant 3$.

presumably has a large magnon-electron interaction, which results in strong damping of the magnon spectra.

To understand the observed spin-wave spectra and the underlying spin-spin interactions, we use linear spin-wave theory (LSWT) with the Hamiltonian, $\mathcal{H} = J_n \sum_{i,j} S_i S_j - D_z \sum_i (S_i^z)^2$, as implemented in the SPINW package [33]. To remove the possible ambiguity of the spin value of a metallic system, we use a generalized parameter representation of spin times exchange SJ_n [29]. J_n and D_z correspond to Heisenberg exchange couplings for the nth nearest neighbor and a single-ion anisotropy, respectively [34]. Interactions up to the fourth- (second-) nearest-neighbor in-plane (out-of-plane) direction (see Fig. 1(a) [Fig. 1(b)]) were considered. Note that SJ_3 and SJ_4 have the same distance but different paths. Hence, the distinction of these parameters is maintained due to the potential effects on the RKKY interaction of the complicated band structure [35]. The measured dispersion is fitted to the calculated dispersion (see Supplemental Material for the fitting [29]), yielding the parameters listed in Table I. The parameters indicate a dominant nearest-neighbor ferromagnetic interaction SJ_1. We also determine non-negligible further neighbor exchanges, SJ_2 ($\sim -0.28SJ_1$), SJ_3 ($\sim 0.12SJ_1$), and SJ_4 ($\sim 0.1SJ_1$), are present. The sign and relative size of the parameters from the spin-wave analysis are largely consistent with parameters determined from first-principles calculations (see Table I). Furthermore, the symmetry-allowed easy-plane single-ion anisotropy ($SD_z > 0$) reproduces the peaked intensity data near 4 meV shown in Fig. 2(d) (see Supplemental Material for further information on single-ion anisotropy [29]).

The refined spin-wave scattering intensity is compared to the experimental data in Figs. 2–4. The calculations reproduce the low-energy spectra. However, the scattering intensity and dispersion deviate from the calculation at the zone boundary and well-defined modes are essentially absent above 200 meV in the measurements. This discrepancy in the scattering intensity is ascribed to interactions with the Stoner continuum [36–39], and indicates the energy scale of the Stoner excitations. Due to the large number of electronic bands in FeSn, it is challenging to make direct comparisons to the magnetic spectra measured here. However, electronic band-structure calculations do indicate the splitting of majority- and minority-spin bands near the Fermi energy [40,41]. The minimum energy of an indirect interband transition near $\mathbf{Q} = \Gamma$ is $\sim$0.1–0.2 eV, which results in a gap of the Stoner excitations with finite momenta [see Fig. 1(e)], and is consistent with the energy scale above which damping begins to dominate the INS spectra.

The determined spin Hamiltonian and the symmetry of the spin configuration preserves time-reversal symmetry, and permit the existence of a Dirac point in the magnon spectrum. LSWT presents a sharp linear magnon band crossing at $E \sim 120$ meV at the K point [see dispersion line in Figs. 3(a) and 3(b)]. Figures 4(a)–4(d) present constant energy slices measured up to 180 meV. The low-energy spectra below the Dirac node are reproduced by LSWT. The Dirac node is evident at the K point at 120 meV as shown in Fig. 4(b). Above 120 meV, the excitations significantly broaden. This is particularly evident near the zone boundary and the broadening increases with increasing energy transfer. Figures 4(e) and 4(f) highlight the dispersion in the vicinity of the Dirac nodes along the transverse and radial directions, respectively. Figure 4(g) shows constant energy scans along the transverse direction through the Dirac nodal point as having two clear peaks below 100 meV and above 150 meV, but only a single peak between 100 and 150 meV in the vicinity of the two crossing bands. Peak positions extracted from Gaussian fits compare well to the LSWT dispersion curve in Fig. 4(e). We note that finite spectral weight, likely due to damping from interactions with the continuum, is present between the two peaks above the Dirac node. In contrast, the momentum scan along the radial direction deviates from the calculated dispersion above 120 meV, as shown in Fig. 4(f). Rather than two peaks, constant energy scans along this direction show a broadened spectral weight centered near the Dirac node. These results demonstrate that the scattering with itinerant electrons reconstructs the upper Dirac cone dispersion, but

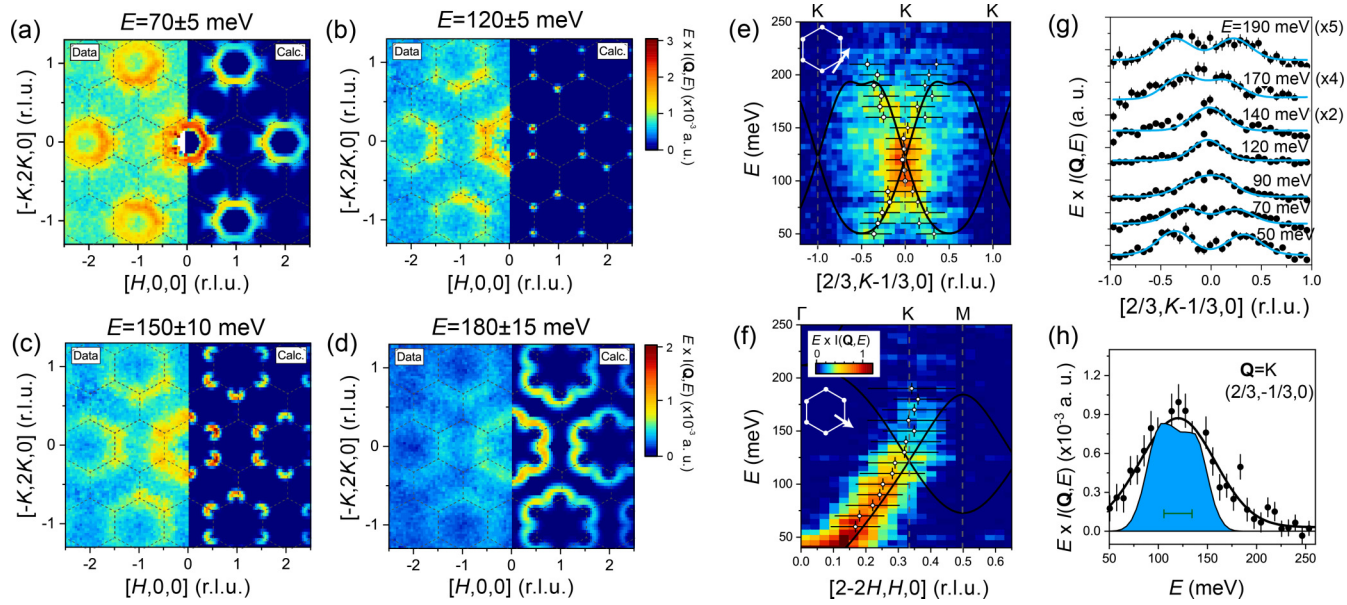

FIG. 4. (a)–(d) Constant energy slices of the INS data [$E \times I(\mathbf{Q}, E)$] and spin-wave calculations. Dashed lines indicate the first BZ in the HK plane. The color bar for (a) and (b) [(c) and (d)] is shown in the right-hand side of (b) [(d)]. INS spectra through the K point along (e) transverse and (f) radial directions (see arrows in insets). (g) Momentum scans at constant energy through the K point along the transverse direction. The dispersion was extracted by fitting the spectra to Gaussian functions (solid lines) and the results are displayed as circles in (e). The lines in (e) and (f) represent the linearly crossing magnons for $L = 0.5$ at the Dirac node. Horizontal (vertical) error bars in (e) and (f) indicate the fitted FWHM (range of energy integration). (h) Constant wave-vector scan at the Dirac point. Data are shown as symbols and the spectral weight from LSWT (shaded region) is described in the text. The line is a guide to eye. Green bar indicates instrumental resolution (FWHM = 28.6 meV) at $E = 120$ meV. The data were obtained by integrating over the momentum region $[0, H, 0] = \pm 0.05$, $[2K, -K, 0] = \pm 0.06$, and $[0, 0, L] = \pm 4$. (e), (f), (h) The nonmagnetic background was obtained from the scattering at $\mathbf{Q} = (2/3, 2/3, 0)$ and subtracted from the measured intensities (see Supplemental Material for the background subtraction [29]).

also the diffusive continuum from the decay fills in the Dirac cone. Figure 4(h) shows an energy scan at the Dirac node compared to the calculated spectral weight of the LSWT model convoluted with the instrumental energy resolution. The decayed spectral weight is visible above 150 meV and extends well beyond the LSWT model of the scattering.

Additionally, the LSWT completely fails to explain the observed upper spectral weight above 120 meV along Γ to M [see Figs. 3(a) and 3(b)]. It is worth noting that a fluctuation continuum is also present at the top of the lower magnon branch at $\mathbf{Q} = M$ (zone boundary) above 80 meV [see Fig. 3(d)]. It connects the lower magnon branch to the upper spectral weight without a gap in the spectrum. This in turn generates a band touching at M around the Dirac node, resulting in a weak ring-shaped spectral weight in the all constant energy slices between 80 and 150 meV (see Fig. 4). This continuous scattering confirms that the excitation near M is not simply due to a spin-wave excitation. Therefore, a likely component of the measured spectral weight near M is the decayed spectra of the upper magnon band. To explain this may require a comparison to the itinerant band model [39,42], a more sophisticated approach which includes the correction from the interactions with itinerant electrons [43,44], or a spin-fermion model [45–47].

In summary, we have found that the spin excitation spectrum in the ferromagnetic kagome metal FeSn is quasi-two-dimensional with progressively stronger damping of the spin waves with increasing energy transfer. The determined exchange terms for the spin Hamiltonian provide for a symmetry-allowed magnon Dirac nodal point near the electronic continua, and the observation of the Dirac magnon in FeSn demonstrates that symmetry plays a key role in determining the magnon topology even in a metallic system. The interaction with the itinerant electrons is large near the nodal point, resulting in a significant spectral broadening with momentum dependence. The interactions are also large near the M point, which result in continuous spectral weight between the lower and upper magnon bands. A more complete understanding of these observations require calculations which account for the electron-magnon interactions. It will

TABLE I. Hamiltonian parameters determined from the LSWT analysis (SJ_{ij}^{Fit}) and first-principles calculation ($SJ_{ij}^{\mathrm{Theory}}$).

Label (number of paths)	SJ_1 (4)	SJ_{int1} (2)	SJ_2 (4)	SJ_{int2} (8)	SJ_3 (2)	SJ_4 (4)	SD_z
SJ_{ij}^{Fit} (meV)	−44.33 ±1.56	4.51 ±1.00	12.23 ±1.06	1.27 ±0.24	−5.28 ±2.32	−4.60 ±0.90	0.1
$SJ_{ij}^{\mathrm{Theory}}$ (meV)	−59.26	14.94	9.04	−3.40	−4.72	1.92	
Distance (Å)	2.65	4.45	4.59	5.18	5.30	5.30	

be particularly interesting to check if the spin-charge coupled spectra in the kagome metallic magnet possesses the topology arising from correlation effects.

Note added. Recently, we became aware of INS work [48] that reports the spin-wave excitations in FeSn.

Acknowledgments. We acknowledge M. Lumsden and J. M. Ok for useful discussions. This research was supported by the U.S. Department of Energy, Office of Science, Basic Energy Sciences, Materials Science and Engineering Division. Work at the Oak Ridge National Laboratory Spallation Neutron Source was supported by U.S. DOE, Office of Science, BES, Scientific User Facilities Division. The neutron experiment at the Materials and Life Science Experimental Facility of the J-PARC was performed under a user program (Proposals No. 2019B0248 and No. 2020A0217).

[1] E. Tang, J.-W. Mei, and X.-G. Wen, Phys. Rev. Lett. **106**, 236802 (2011).
[2] D. N. Sheng, Z.-C. Gu, K. Sun, and L. Sheng, Nat. Commun. **2**, 389 (2011).
[3] T. Neupert, L. Santos, C. Chamon, and C. Mudry, Phys. Rev. Lett. **106**, 236804 (2011).
[4] K. Sun, Z. Gu, H. Katsura, and S. Das Sarma, Phys. Rev. Lett. **106**, 236803 (2011).
[5] J.-X. Yin, S. S. Zhang, H. Li, K. Jiang, G. Chang, B. Zhang, B. Lian, C. Xiang, I. Belopolski, H. Zheng *et al.*, Nature (London) **562**, 91 (2018).
[6] L. Ye, M. Kang, J. Liu, F. Von Cube, C. R. Wicker, T. Suzuki, C. Jozwiak, A. Bostwick, E. Rotenberg, D. C. Bell *et al.*, Nature (London) **555**, 638 (2018).
[7] J.-X. Yin, S. S. Zhang, G. Chang, Q. Wang, S. S. Tsirkin, Z. Guguchia, B. Lian, H. Zhou, K. Jiang, I. Belopolski, N. Shumiya, D. Multer, M. Litskevich, T. A. Cochran, H. Lin, Z. Wang, T. Neupert, S. Jia, H. Lei, and M. Z. Hasan, Nat. Phys. **15**, 443 (2019).
[8] M. Kang, L. Ye, S. Fang, J.-S. You, A. Levitan, M. Han, J. I. Facio, C. Jozwiak, A. Bostwick, E. Rotenberg *et al.*, Nat. Mater. **19**, 163 (2020).
[9] J.-X. Yin, W. Ma, T. A. Cochran, X. Xu, S. S. Zhang, H.-J. Tien, N. Shumiya, G. Cheng, K. Jiang, B. Lian *et al.*, Nature (London) **583**, 533 (2020).
[10] D. J. Thouless, M. Kohmoto, M. P. Nightingale, and M. den Nijs, Phys. Rev. Lett. **49**, 405 (1982).
[11] F. D. M. Haldane, Phys. Rev. Lett. **61**, 2015 (1988).
[12] G. Xu, B. Lian, and S.-C. Zhang, Phys. Rev. Lett. **115**, 186802 (2015).
[13] D. F. Liu, A. J. Liang, E. K. Liu, Q. N. Xu, Y. W. Li, C. Chen, D. Pei, W. J. Shi, S. K. Mo, P. Dudin *et al.*, Science **365**, 1282 (2019).
[14] M. Kang, S. Fang, L. Ye, H. C. Po, J. Denlinger, C. Jozwiak, A. Bostwick, E. Rotenberg, E. Kaxiras, J. G. Checkelsky, and R. Comin, Nat. Commun. **11**, 4004 (2020).
[15] Z. Liu, M. Li, Q. Wang, G. Wang, C. Wen, K. Jiang, X. Lu, S. Yan, Y. Huang, D. Shen, J.-X. Yin, Z. Wang, Z. Yin, H. Lei, and S. Wang, Nat. Commun. **11**, 4002 (2020).
[16] B. R. Ortiz, S. M. L. Teicher, Y. Hu, J. L. Zuo, P. M. Sarte, E. C. Schueller, A. M. Milinda Abeykoon, M. J. Krogstad, S. Rosenkranz, R. Osborn, R. Seshadri, L. Balents, J. He, and S. D. Wilson, Phys. Rev. Lett. **125**, 247002 (2020).
[17] Y. Xing, F. Ma, L. Zhang, and Z. Zhang, Sci. China: Phys., Mech. Astron. **63**, 1 (2020).
[18] S. Owerre, J. Phys. Commun. **1**, 025007 (2017).
[19] A. Mook, J. Henk, and I. Mertig, Phys. Rev. B **89**, 134409 (2014).
[20] R. Chisnell, J. S. Helton, D. E. Freedman, D. K. Singh, R. I. Bewley, D. G. Nocera, and Y. S. Lee, Phys. Rev. Lett. **115**, 147201 (2015).
[21] A. Mook, J. Henk, and I. Mertig, Phys. Rev. B **90**, 024412 (2014).
[22] L. Zhang, J. Ren, J.-S. Wang, and B. Li, Phys. Rev. B **87**, 144101 (2013).
[23] A. Mook, K. Plekhanov, J. Klinovaja, and D. Loss, Phys. Rev. X **11**, 021061 (2021).
[24] P. A. McClarty and J. G. Rau, Phys. Rev. B **100**, 100405(R) (2019).
[25] S. Itoh, T. Yokoo, S. Satoh, S. ichiro Yano, D. Kawana, J. Suzuki, and T. J. Sato, Nucl. Instrum. Methods Phys. Res., Sect. A **631**, 90 (2011).
[26] R. Kajimoto, M. Nakamura, Y. Inamura, F. Mizuno, K. Nakajima, S. Ohira-Kawamura, T. Yokoo, T. Nakatani, R. Maruyama, K. Soyama *et al.*, J. Phys. Soc. Jpn. **80**, SB025 (2011).
[27] The SEQUOIA data is deposited at https://doi.ccs.ornl.gov/ui/doi/395.
[28] G. E. Granroth, A. I. Kolesnikov, T. E. Sherline, J. P. Clancy, K. A. Ross, J. P. C. Ruff, B. D. Gaulin, and S. E. Nagler, J. Phys.: Conf. Ser. **251**, 012058 (2010).
[29] See Supplemental Material at http://link.aps.org/supplemental/10.1103/PhysRevB.105.L180403 for the descriptions of the experimental details, spin-wave analysis, first-principles calculation, instrumental resolution simulation, and single-ion anisotropy, which includes Refs. [28,49–55].
[30] M. E. Zhitomirsky and A. L. Chernyshev, Rev. Mod. Phys. **85**, 219 (2013).
[31] J. Oh, M. D. Le, H.-H. Nahm, H. Sim, J. Jeong, T. Perring, H. Woo, K. Nakajima, S. Ohira-Kawamura, Z. Yamani *et al.*, Nat. Commun. **7**, 13146 (2016).
[32] X. Chen, I. Krivenko, M. B. Stone, A. I. Kolesnikov, T. Wolf, D. Reznik, K. S. Bedell, F. Lechermann, and S. D. Wilson, Nat. Commun. **11**, 3076 (2020).
[33] S. Toth and B. Lake, J. Phys.: Condens. Matter **27**, 166002 (2015).
[34] Indeed, the Dzyaloshinskii-Moriya interaction (DMI) along the z axis (c) is symmetrically allowed. However, since the DMI on the spins aligning in the plane ($z \perp S$) does not change the dispersion, we exclude the DMI in the model Hamiltonian.
[35] L. M. Roth, H. J. Zeiger, and T. A. Kaplan, Phys. Rev. **149**, 519 (1966).
[36] V. Korenman and R. Prange, Phys. Rev. B **6**, 2769 (1972).
[37] S. Ibuka, S. Itoh, T. Yokoo, and Y. Endoh, Phys. Rev. B **95**, 224406 (2017).

[38] C. P. Adams, T. E. Mason, E. Fawcett, A. Z. Menshikov, C. D. Frost, J. B. Forsyth, T. G. Perring, and T. M. Holden, J. Phys.: Condens. Matter **12**, 8487 (2000).
[39] S. O. Diallo, V. P. Antropov, T. G. Perring, C. Broholm, J. J. Pulikkotil, N. Ni, S. L. Bud'ko, P. C. Canfield, A. Kreyssig, A. I. Goldman, and R. J. McQueeney, Phys. Rev. Lett. **102**, 187206 (2009).
[40] Z. Lin, C. Wang, P. Wang, S. Yi, L. Li, Q. Zhang, Y. Wang, Z. Wang, H. Huang, Y. Sun, Y. Huang, D. Shen, D. Feng, Z. Sun, J.-H. Cho, C. Zeng, and Z. Zhang, Phys. Rev. B **102**, 155103 (2020).
[41] B. C. Sales, J. Yan, W. R. Meier, A. D. Christianson, S. Okamoto, and M. A. McGuire, Phys. Rev. Materials **3**, 114203 (2019).
[42] R. A. Ewings, T. G. Perring, J. Gillett, S. D. Das, S. E. Sebastian, A. E. Taylor, T. Guidi, and A. T. Boothroyd, Phys. Rev. B **83**, 214519 (2011).
[43] H. Park, K. Haule, and G. Kotliar, Phys. Rev. Lett. **107**, 137007 (2011).
[44] M. C. T. D. Müller, C. Friedrich, and S. Blügel, Phys. Rev. B **94**, 064433 (2016).
[45] S. Liang, A. Mukherjee, N. D. Patel, C. B. Bishop, E. Dagotto, and A. Moreo, Phys. Rev. B **90**, 184507 (2014).
[46] S. Liang, G. Alvarez, C. Şen, A. Moreo, and E. Dagotto, Phys. Rev. Lett. **109**, 047001 (2012).
[47] S. Liang, A. Moreo, and E. Dagotto, Phys. Rev. Lett. **111**, 047004 (2013).
[48] Y. Xie, L. Chen, T. Chen, Q. Wang, Q. Yin, J. R. Stewart, M. B. Stone, L. L. Daemen, E. Feng, H. Cao *et al.*, Commun. Phys. **4**, 240 (2021).
[49] J. Y. Y. Lin, F. Islam, G. Sala, I. Lumsden, H. Smith, M. Doucet, M. B. Stone, D. L. Abernathy, G. Ehlers, J. F. Ankner, and G. E. Granroth, J. Phys. Commun. **3**, 085005 (2019).
[50] U. von Barth and L. Hedin, J. Phys. C: Solid State Phys. **5**, 1629 (1972).
[51] K. Yamaguchi and H. Watanabe, J. Phys. Soc. Jpn. **22**, 1210 (1967).
[52] Y. Inamura, T. Nakatani, J. Suzuki, and T. Otomo, J. Phys. Soc. Jpn. **82**, SA031 (2013).
[53] O. Arnold, J. Bilheux, J. Borreguero, A. Buts, S. Campbell, L. Chapon, M. Doucet, N. Draper, R. Ferraz Leal, M. Gigg *et al.*, Nucl. Instrum. Methods Phys. Res., Sect. A **764**, 156 (2014).
[54] O. Gunnarsson, O. Jepsen, and O. K. Andersen, Phys. Rev. B **27**, 7144 (1983).
[55] W. Kohn and L. J. Sham, Phys. Rev. **140**, A1133 (1965).

Correction: The previously published Ref. [27] contained an error and has been fixed.